

# Magnetic antenna excitation of whistler modes. 1. Basic Properties

J. M. Urrutia and R. L. Stenzel

*Department of Physics and Astronomy,  
University of California, Los Angeles, CA 90095-1547*

## Abstract

Properties of magnetic loop antennas for exciting electron whistler modes have been investigated in a large laboratory plasma. The parameter regime is that of large plasma frequency compared to the cyclotron frequency and signal frequency below half the cyclotron frequency. The antenna diameter is smaller than the wavelength. Different directions of the loop antenna relative to the background magnetic field have been measured for small amplitude waves. The differences in the topology of the wave magnetic field is shown from measurements of the three field components in three spatial directions. The helicity of the wave magnetic field and of the hodogram of the magnetic vector in space and time are clarified. The superposition of wave fields is used to investigate the properties of two antennas for small amplitude waves. Standing whistler waves are produced by propagating two wave packets in opposite directions. Directional radiation is obtained with two phased loops separated by a quarter wavelength. Rotating antenna fields, produced with phased orthogonal loops at the same location, do not produce directionality. The concept of superposition is extended in a companion paper to generate antenna arrays for whistlers. These produce nearly plane waves, whose propagation angle can be varied by the phase shifting the currents in the array elements. Focusing of whistlers is possible. These results are important for designing antennas on spacecraft or diagnosing and heating of laboratory plasmas.

PACS numbers: 52.35.Hr Electromagnetic waves, 52.50.Dg Plasma interactions with antennas, 94.80.+g Instrumentation for space plasma physics, 94.05.Rx Experimental techniques and laboratory studies, Plasma sources, 52.40.Fd

## I. INTRODUCTION

Antennas are the basic tools for exciting and detecting waves both in free space and in plasmas. Electromagnetic waves can be excited with electric or magnetic antennas. In the present work we are studying waves between the lower hybrid frequency  $\omega_{lh}$  and the electron cyclotron frequency  $\omega_{ce}$ , which are called whistler modes in dense plasmas. These modes are very important in space plasmas where they were first discovered [1]. Since these modes carry most of their energy in the wave magnetic field, it is appropriate to excite them with magnetic loop antennas. These have been studied for a long time but not to the observational detail as presented here [2, 3, 4, 5, 6, 7, 8, 9]. The present work focuses on the field topology excited. A fundamental property of finite size antennas is the excitation of spatial wave packets rather than plane waves, even in unbounded plasmas. The field topology depends on the antenna configuration, but whistler modes always exhibit magnetic helicity and have three field components which vary in space and time. In the present work, a loop antenna is employed whose dipole moment can be oriented at any angle with respect to the ambient field  $\mathbf{B}_0$ . The antenna diameter is smaller than the wavelength and excites monochromatic waves at  $\omega/\omega_{ce} \simeq 0.357$ . The radiation pattern is measured for two orientations of the dipole moment: along and across  $\mathbf{B}_0$ . The polarization of the field vector in space and time is shown for different propagation directions, and is contrasted to the magnetic helicity of the wave. Using superposition for small amplitude waves, the interference effects of multiple antennas are studied. Standing waves are produced from counter propagating whistler mode wavepackets. The standing wave is stationary and helicity-free, and exhibits no absolute field nulls. Two antennas are spaced along  $\mathbf{B}_0$  and properly phased to match a whistler mode produce directional radiation. An antenna with rotating magnetic field has no directionality. In a companion paper, the superposition principle is extended to study phased antenna arrays for whistlers [10]. The results are not only important to antennas on spacecraft but also for helicon plasma sources [11] and rf heating of laboratory plasmas.

This paper is organized as follows: After describing the experimental setup in Section II, the observations are shown in Section III for single loops of different orientations and for two loops by superposition of their individual patterns. The findings are summarized in the Conclusion, Section IV.

## II. EXPERIMENTAL ARRANGEMENT

The experiments are performed in a large (1.5 m diameter, 2.5 m length) dc discharge plasma with parameters of density  $n_e \simeq 10^{11} \text{ cm}^{-3}$ , electron temperature  $kT_e \simeq 2 \text{ eV}$ , and Argon gas pressure  $p \simeq 5 \times 10^{-4} \text{ mTorr}$ . As schematically shown in Fig. 1, the discharge uses a 1 m diam oxide coated hot cathode which is pulsed (5 ms on, 1 s off). The experiments are performed in the early afterglow. A uniform axial magnetic field of 5 G confines the electrons radially. The plasma column is wide compared to the radial wave profile such that density gradients are not significant.

Whistler modes are excited with a 4 cm diam insulated loop antenna which is energized with a 5 MHz signal generator. The loop axis can be continuously rotated with respect to  $\mathbf{B}_0$ . The wave magnetic field is received by a small magnetic probe (6 mm orthogonal loops) which can be moved in three orthogonal directions. The spatial field distribution is obtained from repeated pulses, averaged over 10 shots by moving the probe through orthogonal planes. No data can be taken where the probe would scan through the antenna. The field in vacuum is also measured and subtracted from the total measured field, so as to obtain only the wave field produced by plasma currents. The vacuum field drops off rapidly on the scale of the loop radius ( $B_{\text{vac}} \propto r_{\text{loop}}^{-3}$ ). Plasma parameters are measured with Langmuir probes. All signals are acquired with a 4-channel digital oscilloscope.

## III. EXPERIMENTAL RESULTS

### A. Spatial and temporal wave distributions from a single loop

We start by recalling the wave excitation from a loop antenna whose dipole moment is aligned with  $\mathbf{B}_0$ . Figure 2 shows a snapshot of two orthogonal field components in the  $y$ - $z$  plane on axis ( $x = 0$ ). In vacuum, the loop antenna field is dipolar and symmetric around the  $z$ -axis. The oscillating antenna field excites a modified field topology in plasma. As seen in Fig. 2(a), the axial field component develops  $V$ -shaped contours which are cuts through a cone in three dimensions. The most important feature is the self-consistent development of an orthogonal field component  $B_x$ , shown in Fig. 2(b). The  $B_y$  component has a similar distribution but delayed by a quarter wavelength. By combining both components in the  $x$ - $y$  plane, the orthogonal field forms circular field lines. Thus the dipolar field is linked

by a toroidal field and forms in three dimensions (3D) a spiraling field as in a vortex. It is similar to the  $m = 0$  mode in helicon devices [12, 13], except the conical phase fronts cannot be observed in helicon devices where the plasma radius is that of the antenna which in turn is small compared to the parallel wavelength.

The formation of conical contours or phase fronts can be explained by the decrease of the phase velocity with increasing angle of wave propagation with respect to  $\mathbf{B}_0$ . The normal to the observed cone angle indicates a phase velocity which propagates near the angle  $\theta = \arccos(2\omega/\omega_{ce}) \simeq 44^\circ$ . This mode is known as the Gendrin mode [14, 15]. Its group velocity is aligned with  $\mathbf{B}_0$ , hence there is almost no energy spread across  $\mathbf{B}_0$ .

The reason for the toroidal field is best explained by the frozen-in concept in electron magnetohydrodynamics (EMHD). The dipolar field is created by a toroidal electron Hall current. The associated electron drift convects the axial magnetic field in the toroidal direction. The toroidal field is produced by a dipolar current. Thus the current topology has also a vortex topology. Since current density  $\mathbf{J}$  and field  $\mathbf{B}$  are nearly parallel, the wave field forms a force-free helical structure. Because  $B_x(z)$  reverses sign while  $B_z(z)$  does not, the field line linkage, or magnetic helicity, is positive when the wave propagates along the ambient field, and it is negative for propagation against  $\mathbf{B}_0$ . Likewise, the helicity of the current density ( $\mathbf{J} \cdot \mathbf{B}$ ) changes sign with propagation direction.

The field decomposition into linked poloidal and toroidal components does not convey the actual field lines. These are obtained from the vector field in 3D space, an example of which is given in Fig. 3. It is advantageous to visualize the field as tubes with a constant cross-section centered on field lines instead of single lines. Magnetic flux, therefore, is not conserved for these flux ropes. Two such flux ropes are displayed together with an  $x$ - $y$  plane showing  $B_z$  contours for reference. The flux ropes exhibit a twist around their axis and writhing in loops. The sum of twist and writhe equals linkage and is a measure for the helicity of a flux tube [16]. The vortex-like field topology is similar for each half wavelength, except for a change in field line direction: Near the axis where  $B_z > B_\theta$  the lines have little twist, but when  $B_z \rightarrow 0$  axially the field lines spiral and move radially outward. Field line closure is difficult to identify. Magnetic helicity is positive since both twist and writhe are right handed.

There is no axis of symmetry for the wave field when the loop antenna is rotated such that the dipole field is perpendicular to  $\mathbf{B}_0$ . The observed field components are shown in

Figs. 4(a-c). The distribution of  $B_x$  and  $B_y$  are again conical and shifted by a quarter wavelength. Following the peaks of the field components axially along the dashed white line one realizes a circular polarization. The  $B_z$  component vanishes on the  $z$ -axis and reverses sign in both  $y$  and  $z$  directions.

The 3D field topology is shown in Fig. 5. Contours of  $B_z$  are displayed in Fig. 5(a) and field lines are traced in one of the field maxima. Since all field lines rotate in space, the field line develops a spiral with pitch length of the axial wavelength. A second spiral forms in the negative peaks of  $B_z$ , resulting in two nested helices with opposite field line directions as shown in the full 3D view of Fig. 5(b). The flux ropes have a left-handed writhe and a right-handed twist. The twist exceeds one turn ( $\text{twist} > 1$ ) for one rotation of the spiral (writhing number =  $-1$ ) such that the net magnetic helicity of the flux rope becomes positive. The spiral flux tubes rotate clockwise in time. When a magnetic probe is scanned axially through the spirals, it observes a highly modulated amplitude  $|B_z|$  with peaks separated by  $\lambda/2$  [13].

The current density  $\mathbf{J} = \nabla \times \mathbf{B}/\mu_0$  is calculated from the 3D  $\mathbf{B}$  field. Its topology is very similar to that of the  $\mathbf{B}$  field, which was also found for the loop with dipole moment along  $\mathbf{B}_0$ . Figure 5(c) displays a flux tube for  $\mathbf{J}$  which form two twisted spirals with currents flowing in opposite directions. The current density also exhibits positive helicity since the twist is stronger than the writhe. The helicity density  $\mathbf{J} \cdot \mathbf{B}$  is shown in Fig. 5(d). It is positive in the right half-plane where the wave propagates along  $\mathbf{B}_0$ , and negative in the left half-plane for the opposite propagation direction. Since  $\mathbf{J}$  is parallel to  $\mathbf{B}$ , the wave field is force-free,  $\mathbf{J} \times \mathbf{B} = 0$ .

It is easy to show for plane parallel whistlers that  $\nabla \times \mathbf{B} = \pm k\mathbf{B}$ , hence  $\mathbf{J}$  is parallel to  $\pm\mathbf{B}$ . Likewise the magnetic helicity density is  $\mathbf{A} \cdot \mathbf{B} = \pm\mu_0 B^2/k$ . It is remarkable that the helical fields and currents of the oblique whistler mode also satisfies  $\mathbf{J} \parallel (\pm\mathbf{B})$  to a high degree.

The mode excited by the loop dipole moment across  $\mathbf{B}_0$  has similarity to the  $m = 1$  helicon mode [17] in bounded plasma columns. In the present experiment, the perpendicular wave number is not determined by the column diameter but approximately by the scale length of the antenna field. In an unbounded plasma, the excited whistler mode is free to evolve to a self-consistent topology which appears to be a conical Gendrin mode. The phase fronts are inclined with respect to  $\mathbf{B}_0$  unlike those postulated for helicons.

The fields always exhibit right-handed polarization like free space whistlers and there is

no  $m = -1$  mode which has been conjectured for helicons [11]. The reason for the right-handed polarization goes back to Faraday's law,  $\nabla \times \mathbf{E} = -\partial \mathbf{B}/\partial t$ , and Ohm's law in ideal electron magnetohydrodynamics (EMHD),  $\mathbf{E} + \mathbf{v} \times \mathbf{B} = 0$ , which describes the convection of field lines by an electron drift  $\mathbf{v}$ ,  $\partial \mathbf{B}/\partial t = \nabla \times (\mathbf{v} \times \mathbf{B})$ .

Consider in Fig. 6 a wave field  $B_y$  driven by Hall currents  $\pm J_x$ , all propagating along  $\mathbf{B}_0$ . The associated electron drift  $\mp v_x$  creates an electric field  $(\mathbf{v} \times \mathbf{B}_0)_y$  which has a curl in  $x$ -direction, hence produces  $\partial B_x/\partial t$  which rotates the  $B_y$  vector counter-clockwise. Alternatively, the flow  $v_x$  convects the frozen-in field  $\mathbf{B}_0$  out of the  $y$ - $z$  plane which creates a  $B_x$  field component.

The convection equation also describes wave propagation and the dispersion relation. Consider  $B_y$  propagating as a monochromatic wave along  $\mathbf{B}_0$ , written as  $B_y = b \cos(\omega t - kz)$  where  $b$  is the wave amplitude. The linearized wave equation,  $\partial \mathbf{B}/\partial t = \nabla \times (\nabla \times \mathbf{B} \times \mathbf{B}_0)/(-\mu_0 ne)$ , yields  $\partial B_x/\partial t = b \cos(\omega t - kz) k^2 B_0 / \mu_0 ne = \omega B_y$ . After time integration, one finds  $B_x = b \sin(\omega t - kz) k^2 B_0 / (\omega \mu_0 ne) = b \sin(\omega t - kz)$ . Thus,  $B_x$  leads spatially over  $B_y$  which results from the time derivative in the convection equation. The wave dispersion is given by Fourier transformation of the wave equation,  $\omega = k^2 B_0 / (\mu_0 ne)$ , which can be further condensed by the refractive index relation  $n^2 = \omega_{pe}^2 / (\omega \omega_{ce})$ .

Note that  $\mu_0 \mathbf{J} = \nabla \times \mathbf{B} = k \mathbf{B}$  and the vector potential is  $\mathbf{A} = k^{-1} \mathbf{B}$ . Thus the field has positive helicity densities  $\mathbf{A} \cdot \mathbf{B}$  and  $\mathbf{J} \cdot \mathbf{B}$  for propagation along  $\mathbf{B}_0$  ( $k > 0$ ) and negative helicities for propagation opposite to  $\mathbf{B}_0$  ( $k < 0$ ). Although the field lines are straight, their rotation along  $\mathbf{B}_0$  accounts for the helicity. The field is also force-free,  $\mathbf{J} \times \mathbf{B} = 0$ . The scale length of the field is given by the wavelength,  $\mathbf{A} \cdot \mathbf{B} / B^2 = 1/k = \lambda/2\pi$ . These results only hold for the simplest whistler mode, i.e. plane, low frequency, parallel and small amplitude whistlers.

Finally, we would like to review the sometimes confusing concepts of polarization and helicity. The former refers to the rotation of a vector in time or space [18], while helicity refers to the property of a field line, such as its twist, writhe and linkage [16]. Figure 7 describes the polarization (a) in space and (b) in time both schematically and from observations. From the measured field components  $B_x$  and  $B_y$  in Fig. 4, one can sketch the vector rotation along the  $z$ -axis on both sides of the loop. It shows that the end point of the vector forms a left handed spiral or hodogram along  $\mathbf{k}$  for wave propagation along  $\mathbf{B}_0$  and a right handed curve along  $-\mathbf{z}$  direction for propagation opposite to  $\mathbf{B}_0$ . Two measured hodograms confirm the

expected polarization.

The temporal polarization describes the vector rotation in time at a fixed position as the wave passes through the point of observation. If time was plotted along the  $z$ -axis, the vector tip would trace out a right handed helix, irrespective of the direction of wave propagation along  $\mathbf{B}_0$ . The right handed polarization is explained in Fig. 6. It coincides with the direction of rotation of electrons around the guide magnetic field  $\mathbf{B}_0$  because the  $e\mathbf{v} \times \mathbf{B}$  force determines both the electron rotation and field convection. It also allows Doppler-shifted cyclotron resonance between the wave electric field and electrons to occur. Note that the present wave is not a plane wave and that the temporal polarization changes with position which makes single-point measurements, as made by spacecraft, difficult to interpret.

In order to demonstrate the wave propagation, the space-time dependence of the fields is measured. Figure 8 shows time-of-flight diagrams of the transverse field component  $B_y(z, t)$  in the central  $y$ - $z$  plane ( $x = 0$ ) in (a) the early afterglow and (b) the late afterglow. It includes the turn-on phase and the steady-state phase of the wave so as to compare group and phase velocities. The inclination of the phase fronts (contours of  $B_y = 0$  or  $B_{y,\max}$ ) yields the parallel phase velocity,  $v_z \simeq 8 \times 10^7$  cm/s. The transient turn-on oscillations, which should travel at the group velocity, have the same velocity,  $v_{\text{group}} = v_{\text{phase},\parallel} = c\omega_{ce}/(2\omega_{pe})$ , which is the property of the oblique Gendrin mode [14]. This mode propagates at an angle  $\theta = \arccos(2\omega/\omega_{ce})$  with respect to  $\mathbf{B}_0$  at a phase velocity  $v_{\text{phase}} = v_{\text{phase},\parallel} \cos \theta = c\omega/\omega_{pe}$ . This mode evolves self-consistently right after wave injection. The frequency-independent group velocity yields a simple measure for the plasma density which is indicated in Figs. 8(a) and (b).

The parallel phase velocity is comparable to the electron thermal speed which has consequences on wave damping. In general, the axial amplitude decay can arise from collisional damping, wave-particle interactions and radial wave spread. Coulomb collisions ( $\nu_{ei} \simeq 10^6$  s $^{-1}$ ) cannot account for the observed amplitude decay,  $k_i/k_r \simeq 0.2 \gg (v_{\text{phase}}/v_{\text{group}})(\nu/\omega) \simeq 0.03$ . Wave spread is small since the group velocity angle is within  $\pm 5^\circ$  of  $\mathbf{B}_0$ . But since the oblique whistler mode has a parallel electric field, Landau damping ( $\omega/k = v_e$ ) by bulk electrons is important. Cyclotron damping [ $(\omega - \omega_{ce})/k_{\parallel} = v_e$ ] involves fast tail electrons which are absent since the experiment is done in a Maxwellian afterglow plasma. Nonlinear effects and mode conversions at gradients are also absent.

## B. Wave interference from two loop antennas: Whistler standing waves

The applied signal to the antenna produces small amplitude whistlers which is confirmed by a linear scaling between waves and antenna currents. Thus, linear superposition of wave fields is permissible. Instead of using two physical antennas, the data of one antenna can be shifted in space and superimposed to obtain the wave packet propagation of two or more antennas. The first example will show the interference of whistler modes excited by two loops at opposite ends of the measurement plane,  $z = 0$  and  $z = 35$  cm.

Figure 9 shows a comparison between the fields excited by a single loop and by two loops. The latter is obtained by adding the left propagating wave of the single loop [see Fig. 2(a)] to the right propagating wave. Therefore only the plane between the antennas is shown. The loop axis is oriented along the dc magnetic field but similar results are obtained for the orthogonal loop orientation.

Figures 9(a,b) show that, although the wave is damped, the amplitudes of the counter-propagating waves are comparable in the center region and form nearly perfect standing waves for  $B_z$ . Since the  $B_z$  components of both antennas have the same sign, they add at the geometric center forming a maximum or antinode. Nodes in  $B_z$  (nulls) are formed at  $\lambda/4$  adjacent to the maxima.

The dipolar field is linked by a toroidal field. Figures 9(c,d) show the interference of the transverse field component  $B_x$ .  $B_y$  has similar properties since both form the toroidal field. Since the toroidal field direction depends on the propagation direction with respect to  $\mathbf{B}_0$ , the two opposing toroidal fields cancel at the center where the axial fields add. The toroidal fields add where  $B_z$  has nulls and vice versa (see dashed lines). Thus, the standing wave has no field line linkage or helicity in contrast to the propagating wave. Standing waves do not satisfy the force-free condition of traveling whistler modes, hence the  $\mathbf{J} \times \mathbf{B}$  term may produce nonlinear wave-wave interactions. For wave amplitudes exceeding the ambient field, the wave fields merge forming a field-reversed configuration (FRC) for the total magnetic field which has been studied earlier [19].

The whistler standing wave produces no complete field cancelation because the nodes in  $B_z$  and  $B_\theta$  occur at different locations. The interference is also complicated by the conical phase fronts which prevent total constructive or destructive interference off-axis. Wave reflection from conducting boundaries produces even less amplitude modulation since the



reflected wave is usually smaller than the incident wave.

Figures 9(e,f) show the total wave amplitude  $|B| = (B_x^2 + B_y^2 + B_z^2)^{1/2}$  on axis ( $x = y = 0$ ) vs time. For a single antenna located at  $z = 0$ , the field propagates away and damps before reaching the ends of the chamber such that standing waves due to end wall reflections do not arise. For two antennas at  $z = 0$  and  $z = 35$  cm, the fields from both sources propagate toward the center ( $z = 17$  cm) where they repeatedly form amplitude maxima and minima. The modulation depth is largest on axis where the toroidal field vanishes.

### C. Directional radiation from two loop antennas

When two antennas are placed close to each other, the interference can produce different amplitudes on the two sides of the antenna, i.e. produce asymmetric radiation with respect to  $\mathbf{B}_0$ .

The most effective method to produce high directionality is by assembling an antenna configuration resembling the topology of the wave inside the plasma. This can be accomplished by placing two antennas spaced axially apart by  $\lambda/4$ , one exciting a  $B_x$  component, the other a  $B_y$  component. The antennas can be rotated by  $90^\circ$  and fed in phase or by two antennas without rotation but fed by currents with a  $90^\circ$  phase shift. The phase shift between  $B_x$  and  $B_y$  determines the preferred direction of wave propagation. The antenna should be smaller than the wavelength, otherwise the antennas overlap and couple. The present antenna diameter is about  $\lambda/3$ .

Figure 10 shows the superposition of fields from two loop antennas with the same direction of the dipole moment ( $\perp \mathbf{B}_0$ ) and a  $90^\circ$  phase lag between the antenna currents. Both the axial field  $B_z$  [Fig. 10(a)] and the transverse field  $B_y$  [Fig. 10(b)] as well as the total field strength  $|B|$  [Fig. 10(c)] show a high asymmetry in  $\pm z$ -direction. This phased antenna radiates preferentially in  $+z$ -direction with an amplitude ratio  $B_{\max}/B_{\min} \simeq 8$ , i.e., a power ratio of 64 or 18 dB. Phase reversal switches the preferred radiation into the  $-z$  direction. The same directionality is obtained when the two antennas are fed in phase, separated axially by  $\lambda/4$  but one loop is rotated by  $90^\circ$ .

Earlier experiments have reported antenna directionality [20, 21]. The antennas consisted of a current knot or a torus with a linked loop through the center. Such antennas produced helical fields matching the helicity of whistler waves. It was argued that helicity injection and

conservation creates the antenna directionality. The present experiments show that antennas without current linkage also produce directionality. Figure 11 compares two phased loops with different directions of dipole moments. For orthogonal dipole moments [Fig. 11(a)], it could be argued that two phased loops still inject helicity since their combined field is twisted. But for dipole moments parallel to  $\mathbf{B}_0$  [Fig. 11(b)], the resultant antenna field has no helicity, yet the phase shift produces directionality. The simplest explanation for producing directionality is that the antenna has to produce a traveling field which matches that of the whistler mode. The latter has both  $B_z$  and  $B_\perp$  fields and the antenna can match to either or both of them.

In principle, several loops can be stacked as an end-fire array like Yagi antennas [22], but observations show that even a third antenna does not significantly improve the directionality. The antennas must be spaced  $\lambda/4$  apart. Two antennas spaced  $\lambda/2$  apart and phase shifted by  $180^\circ$  do not produce directionality since they do not distinguish between the sense of rotation of the spatial polarization.

Many helicon antennas are  $\lambda/2$  long [17]. Magnetic antennas with helicity are also employed for helicon sources [11]. Strong coupling, hence efficient ionization, is observed when the antenna field topology matches that of the  $m = 1$  helicon mode in a plasma column. Since the antenna is usually placed at the end of the plasma column, the property of antenna directionality has apparently escaped attention.

It should be pointed out that the same loop arrays can also be used as receiving antennas. They possess directionality, but reciprocity does not hold. For example, a directional antenna which transmits along  $\mathbf{B}_0$  produces a large received signal in an identical antenna at some distance along  $\mathbf{B}_0$ . But when the receiving antenna is chosen as an exciter and the original exciter as a receiving antenna, no transmission is possible since the direction of wave propagation is reversed. Both antennas would have to reverse their phasing to permit transmission in the opposite direction.

#### D. Rotating antenna fields

Circularly polarized waves are excited in free space with either crossed electric dipoles or crossed magnetic loops. The dipole signals are phase shifted by  $90^\circ$  and produce a rotating field. Since the whistler mode is a circularly polarized electromagnetic wave, it is natural to

use right-hand rotating magnetic fields for efficient wave excitation [8], plasma production [17], and confinement [23]. We can easily evaluate here the properties of a rotating-field antenna by superimposing the fields of two loop antennas at the same location, rotated by  $90^\circ$  and phase shifted by  $90^\circ$ . The present focus is on the antenna coupling to whistler modes in a uniform plasma. The dipole moments of the loops are orthogonal to  $\mathbf{B}_0$ .

Figure 12 shows vectors of the transverse field ( $B_x, B_y$ ) and contours for the total field strength  $|\mathbf{B}|$  in  $x$ - $y$  planes at a fixed time for different conditions. Figure 12(a) shows, for a right-handed rotation of the antenna field, a strong dipole field, predominantly in  $x$ -direction, and an azimuthally uniform distribution of the total field strength at  $\Delta z = 18$  cm from the antenna. For a left-handed rotation of the antenna field, Fig. 12(b) shows a weak wave field because the applied field rotation is opposite to the polarization of the whistler mode.

There is no phase shift in Fig. 12(c) between the two orthogonal loops, hence the antenna field is linearly polarized at  $45^\circ$  with respect to either loop. The received wave amplitude is almost as strong as that excited by the rotating antenna. A rotating antenna offers little improvement over a linearly polarized one.

Figure 12(d) shows once more the wave field from the rotating antenna but now in an  $x$ - $y$  plane on the opposite side of the antenna ( $\Delta z \simeq -12$  cm). The strong signal shows that the rotating antenna excites waves in both directions along  $\mathbf{B}_0$ , i.e. is not directional. The vector rotation and slight increase in field strength are due to the closer distance to the antenna. In conclusion, the largest waves are excited by directional antennas.

#### IV. CONCLUSION

Basic properties of magnetic loop antennas have been presented for exciting low frequency whistler modes. The wave field topology is shown for different directions of the antenna dipole moment with respect to  $\mathbf{B}_0$ . Spatial wave packets are launched whose fields have three components that vary in space and time. When the antenna dipole moment is along  $\mathbf{B}_0$ , the induced field resembles a vortex with linked poloidal (dipolar) and toroidal fields. When the dipole is aligned across  $\mathbf{B}_0$ , a transverse field is excited which rotates with circular polarization. The transverse and axial field components combine in 3D to form two opposing flux tubes which spiral around  $\mathbf{B}_0$ . The field lines exhibit right-handed twist and left-handed

writhe. The two modes resemble the  $m = 0$  and  $m = 1$  bounded helicon modes but are not caused by boundary effects.

As the waves propagate away from the antenna, the phase fronts assume a conical shape since oblique propagation is slower than parallel propagation. The cone angle suggests oblique wave propagation in the Gendrin mode whose group velocity is field aligned. The wave is axially damped predominantly by Landau damping and Coulomb collisions. Whistler modes possess magnetic helicity whose sign is positive (negative) for propagation along (opposite to)  $\mathbf{B}_0$ . The spatial polarization of the rotating field vector along  $\mathbf{B}_0$  also changes sign, but the temporal polarization is always right-handed.

The field of two or more antennas is obtained by superposition of linear waves excited at different antenna locations. Whistler standing waves have been produced with counter-propagating whistler modes which is a different approach than by wave reflection from conducting boundaries [24]. The transverse and axial field components interfere constructively and destructively at different locations such that no absolute field nulls arise. The standing wave has no helicity and assumes an FRC topology for large amplitudes [19].

A whistler Yagi-type (end-fire array) array antenna is investigated, using a minimum of two phased loops spaced a quarter wavelength apart along  $\mathbf{B}_0$ . When the antenna field matches that of a whistler mode, a strong wave is excited in one direction but not in the opposite direction. The directionality is not due to helicity injection. Directional whistler antennas are not reciprocal for transmitting and receiving [20, 21]. An antenna with rotating field produces no directionality.

The main conclusion is the importance of measuring three field components in 3D space to assess the antenna or wave properties correctly. Single point measurements as, for example, on spacecraft cannot establish whether the wave is a plane wave or a wave packet. Single component measurements cannot identify the field topology. For wave packets, plane wave theory is hardly applicable when the gradient scales of the plasma or magnetic field are comparable to the wavelength. Interference of whistler modes yields wave packets with locally varying polarizations.

In most laboratory experiments reported so far only single antennas have been used. The present work shows that interference effects between multiple antennas can produce useful applications. We will show in the companion paper [10] that antenna arrays can produce nearly plane whistler waves, whose angle of propagation can be varied by phasing. Also,

different directions of group and phase velocities can be produced, suggesting that wave focusing is possible.

## Acknowledgments

The authors gratefully acknowledge support from NSF/DOE grant 20101721.

- 
- [1] H. Barkhausen, *Physik. Z.* **20**, 401 (1919).
  - [2] T. Wang and T. Bell, *J. Geophys. Res.* **77**, 1174 (1972), URL <http://dx.doi.org/10.1029/JA077i007p01174>.
  - [3] D. R. Baker and T. A. Hall, *Plasma Physics* **16**, 901 (1974), URL <http://dx.doi.org/10.1088/0032-1028/16/10/002>.
  - [4] R. L. Stenzel, *Radio Sci.* **11**, 1045 (1976), URL <http://dx.doi.org/10.1029/RS011i012p01045>.
  - [5] A. V. Kostrov, A. V. Kudrin, L. E. Kurina, G. A. Luchinin, A. A. Shaykin, and T. M. Zaboronkova, *Phys. Scripta* **62**, 51 (2000), URL <http://dx.doi.org/10.1238/Physica.Regular.062a00051>.
  - [6] W. E. Amatucci, D. D. Blackwell, D. N. Walker, G. Gatling, and G. Ganguli, *IEEE Trans. Plasma Sci.* **33**, 637 (2005), URL <http://dx.doi.org/10.1109/TPS.2005.844607>.
  - [7] M. E. Gushchin, S. V. Korobkov, A. V. Kostrov, A. V. Strikovskiy, T. M. Zaboronkova, C. Krafft, and V. A. Koldanov, *Phys. Plasmas* **15**, 053503 (2008), URL <http://dx.doi.org/10.1063/1.2907784>.
  - [8] A. V. Karavaev, N. A. Gumerov, K. Papadopoulos, X. Shao, A. S. Sharma, W. Gekelman, A. Gigliotti, P. Pribyl, and S. Vincena, *Phys. Plasmas* **17**, 012102 (2010), URL <http://dx.doi.org/10.1063/1.3274916>.
  - [9] J. P. Pfannmoeller, C. Lechte, O. Grulke, and T. Klinger, *Phys. Plasmas* **19**, 102113 (2012), URL <http://dx.doi.org/10.1063/1.4763558>.
  - [10] R. L. Stenzel and J. M. Urrutia, companion paper 2, submitted to *Phys. Plasmas* (2014), URL <http://www.physics.ucla.edu/plasma-exp/references/publications/PoP/WAntennas-2.pdf>.
  - [11] F. F. Chen, *Phys. Plasmas* **3**, 1783 (1996), URL <http://dx.doi.org/10.1063/1.871697>.
  - [12] G. R. Tynan, A. D. Bailey, III, G. A. Campbell, R. Charatan, A. de Chambrier, G. Gibson,

- D. J. Hemker, K. Jones, A. Kuthi, C. Lee, et al., J. Vac. Sci. Technol. A **15**, 2885 (1997), URL <http://dx.doi.org/10.1116/1.580844>.
- [13] C. M. Franck, O. Grulke, A. Stark, T. Klinger, E. E. Scime, and G. Bonhomme, Plasma Sources Sci. Technol. **14**, 226 (2005), URL <http://dx.doi.org/10.1063/1.1602697>.
- [14] R. Gendrin, Planet Space Sci. **5**, 274 (1961), URL [http://dx.doi.org/10.1016/0032-0633\(61\)90096-4](http://dx.doi.org/10.1016/0032-0633(61)90096-4).
- [15] R. A. Helliwell, *Whistlers and Related Ionospheric Phenomena* (Stanford University Press, Stanford, CA, 1965).
- [16] M. A. Berger, in *Magnetic Helicity in Space and Laboratory Plasmas*, edited by M. R. Brown, R. C. Canfield, and A. A. Pevtsov (Am. Geophys. Union (Washington, DC), 1999), no. 111 in Geophys. Monograph, pp. 1–9, URL <http://dx.doi.org/10.1029/GM111p0001>.
- [17] R. W. Boswell, Plasma Physics and Controlled Fusion **26**, 1147 (1984), URL <http://dx.doi.org/10.1088/0741-3335/26/10/001>.
- [18] Y. Narita, G. Kleindienst, and K.-H. Glassmeier, Ann. Geophys. **27**, 39673976 (2009), URL [www.ann-geophys.net/27/3967/2009/](http://www.ann-geophys.net/27/3967/2009/).
- [19] R. L. Stenzel, J. M. Urrutia, and K. D. Strohmaier, Phys. Plasmas **15**, 042307 (2008), URL <http://dx.doi.org/10.1063/1.2903065>.
- [20] C. L. Rousculp and R. L. Stenzel, Phys. Rev. Lett. **79**, 837 (1997), URL <http://dx.doi.org/10.1103/PhysRevLett.79.837>.
- [21] R. L. Stenzel, J. M. Urrutia, and M. C. Griskey, Phys. Plasmas **6**, 4450 (1999), URL <http://dx.doi.org/10.1063/1.873731>.
- [22] H. Yagi, Proceedings of the IEEE **85**, 1864 (1997), URL <http://dx.doi.org/10.1109/JPROC.1997.649674>.
- [23] T. S. Huang, Y. Petrov, and F. Zhong, Plasma Phys. Control. Fusion **47**, 1517 (2005), URL <http://dx.doi.org/10.1088/0741-3335/47/9/010>.
- [24] W. Amatucci, D. Blackwell, E. Tejero, C. Cothran, L. Rudakov, G. Ganguli, and D. Walker, IEEE Transactions on Plasma Science **39**, 637 (2011), URL <http://dx.doi.org/10.1109/URSIGASS.2011.6051181>.

## Figures

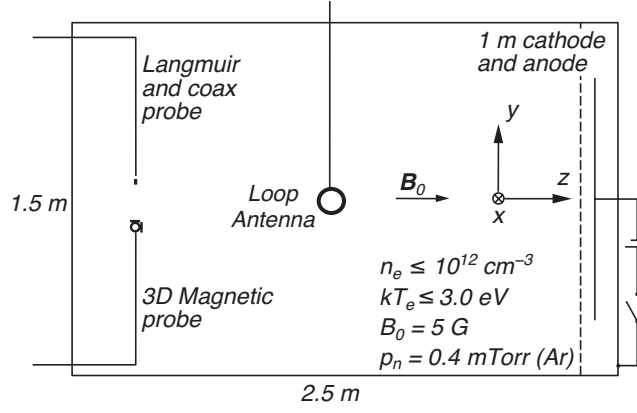


FIG. 1: Schematic diagram of the experimental setup with basic plasma parameters.



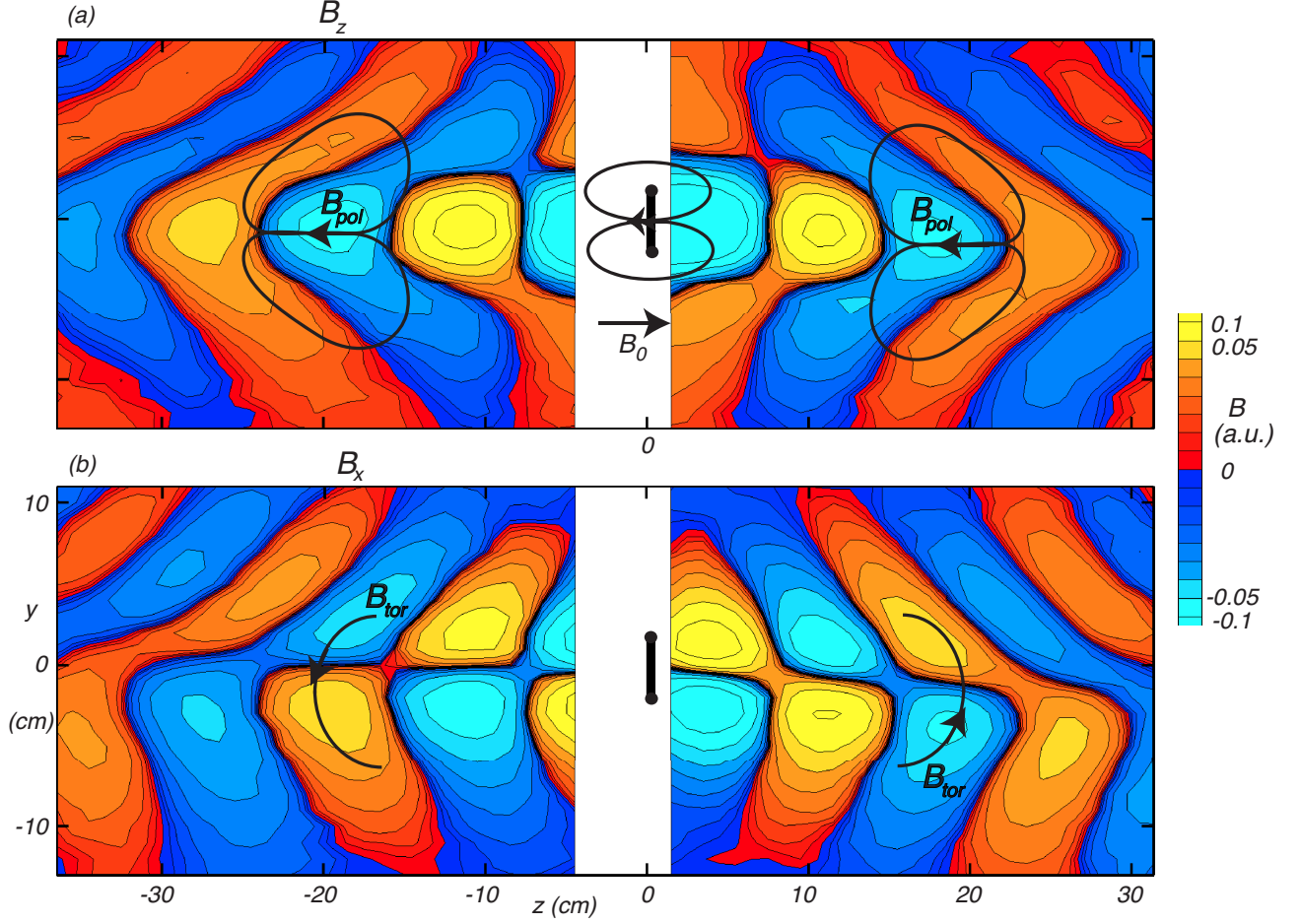


FIG. 2: Fields of a whistler mode excited by a loop antenna whose dipole moment is aligned with the uniform guide field  $\mathbf{B}_0$ . (a) Snapshot of the axial field component  $\mathbf{B}_z(0, y, z)$ . Black lines indicate the poloidal (dipolar) field similar to the loop field. (b) Snapshot of the transverse field component  $\mathbf{B}_x(0, y, z)$ . The third component  $\mathbf{B}_y(0, y, z)$  is as in (b) but shifted by  $\lambda/4$ . The perpendicular field forms a toroidal field, indicated by black lines, which links with the toroidal field so as to produce positive magnetic helicity for  $z > 0$  and negative helicity for  $z < 0$ . Scale varies by a factor 2 per contour.

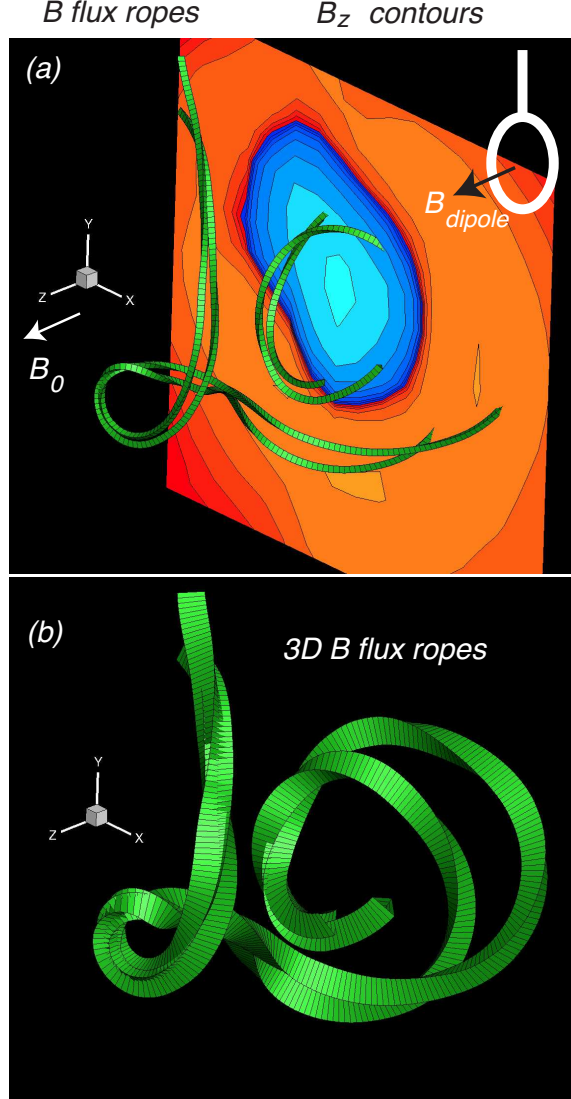


FIG. 3: Magnetic field topology of wave fields excited by a loop antenna with dipole moment along  $\mathbf{B}_0$ . (a) 3D view of two field lines intersecting a plane with contours of  $B_z$ . The field lines exhibit both twist and writhe which is better seen by a 3D flux rope displayed in (b). The flux ropes have a constant triangular cross section which shows a right-handed twist around the guiding center. The two ropes also twist around each other. The writhe is also right-handed, indicating positive magnetic helicity for the wave which propagates along  $\mathbf{B}_0$ .

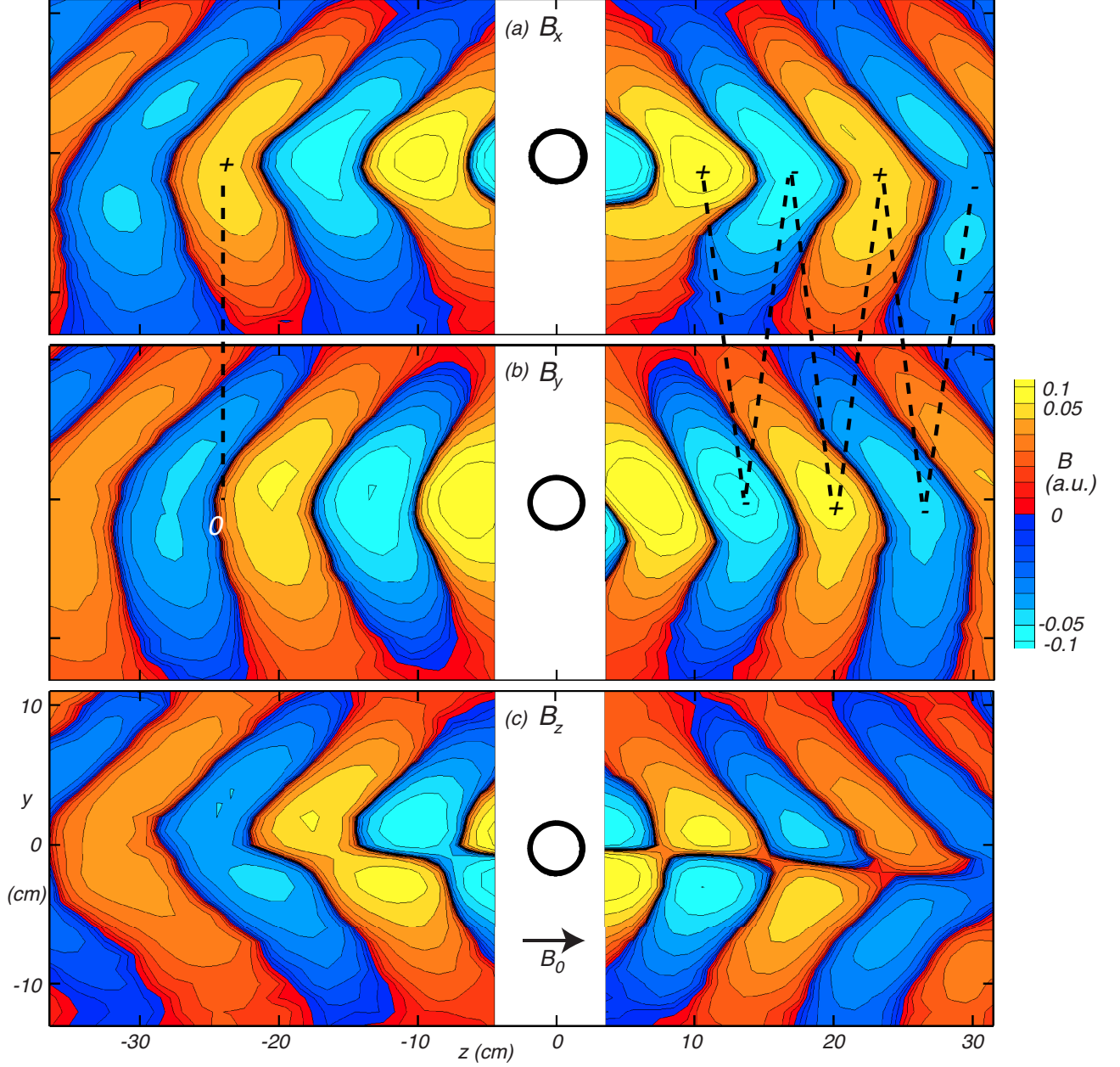


FIG. 4: Fields of a whistler mode excited by a loop antenna whose dipole moment is aligned perpendicular to the uniform guide field  $\mathbf{B}_0$ . (a-c) Three field components are shown at a fixed time in the central  $y$ - $z$  plane ( $x = 0$ ). The phase fronts are conical and the phase velocity angle is close to the Gendrin angle,  $\arccos(2\omega/\omega_{ce}) \simeq 44^\circ$ .

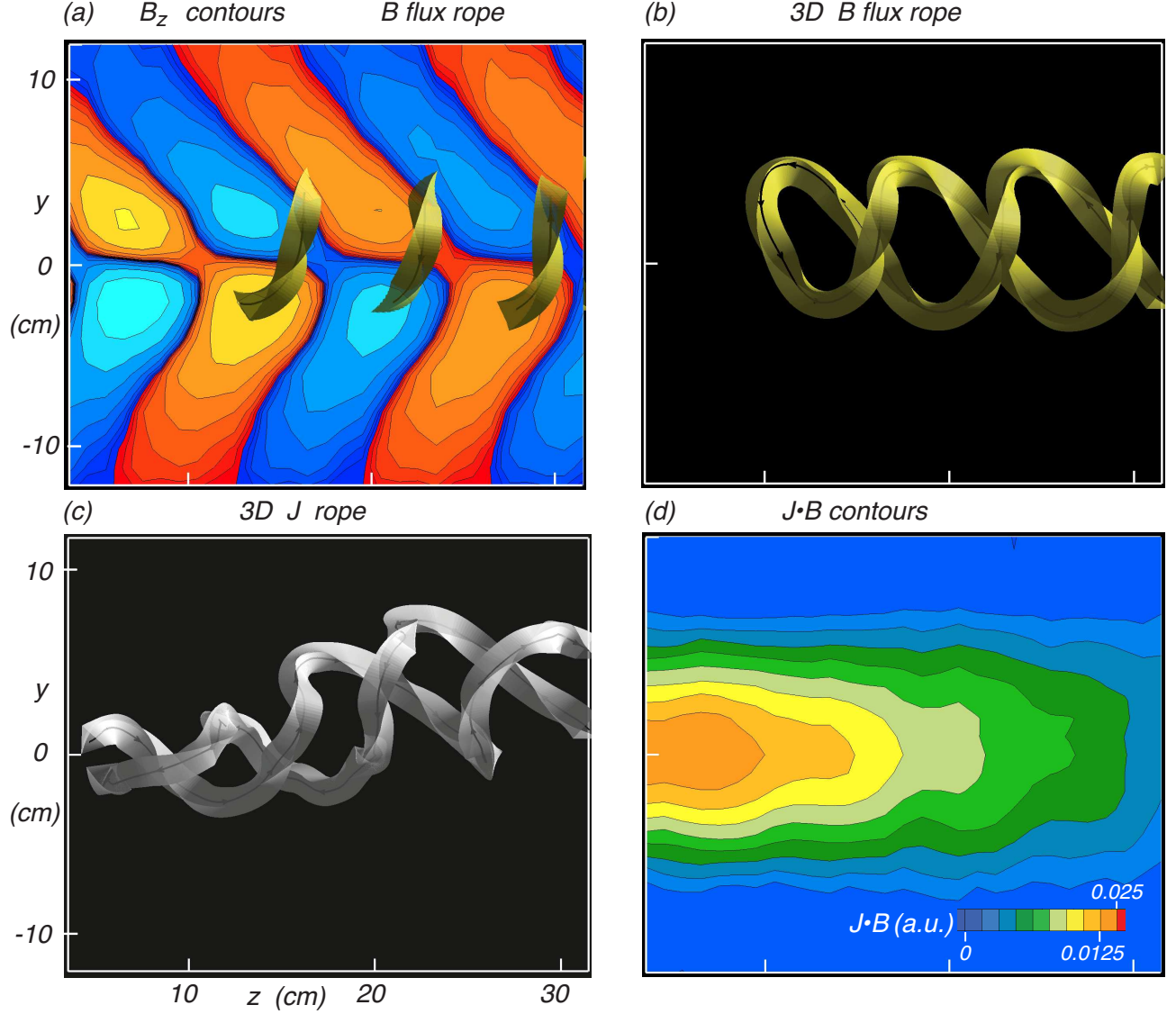


FIG. 5: Field topology of whistler modes excited by a loop antenna with dipole moment orthogonal to  $\mathbf{B}_0$ . (a) Contours of  $B_z(y, z)$  and a 3D flux rope penetrating the  $x = 0$  plane. (b) The same flux rope without the contour plane showing that it consists of two left-handed helices with field lines in opposite directions. Note that the flux ropes have a right-handed twist. (c) 3D ropes of the current density  $\mathbf{J} = \nabla \times \mathbf{B}/\mu_0$ , also forming two opposing left-handed helices. (d) Contour plot of  $\mathbf{J} \cdot \mathbf{B}$  showing a positive sign, i.e.  $\mathbf{J} \parallel \mathbf{B}$  or the helicity of the current density is positive.

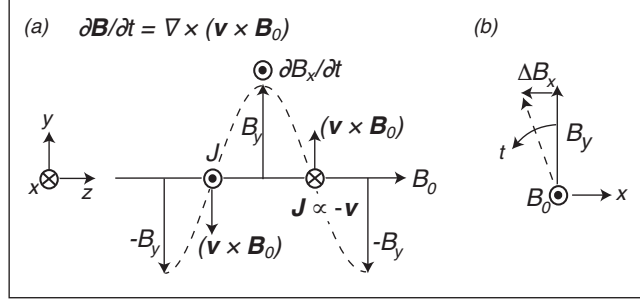


FIG. 6: Schematic figure explaining the rotation of  $\mathbf{B}_\perp$  in EMHD plasmas by convection of frozen-in field lines. The field vector  $B_y$  is associated with electron drifts  $v_x$  which produces a motional electric field with a curl in  $x$ -direction. This creates a field in  $-x$ -direction which rotates  $B_y$  counterclockwise.

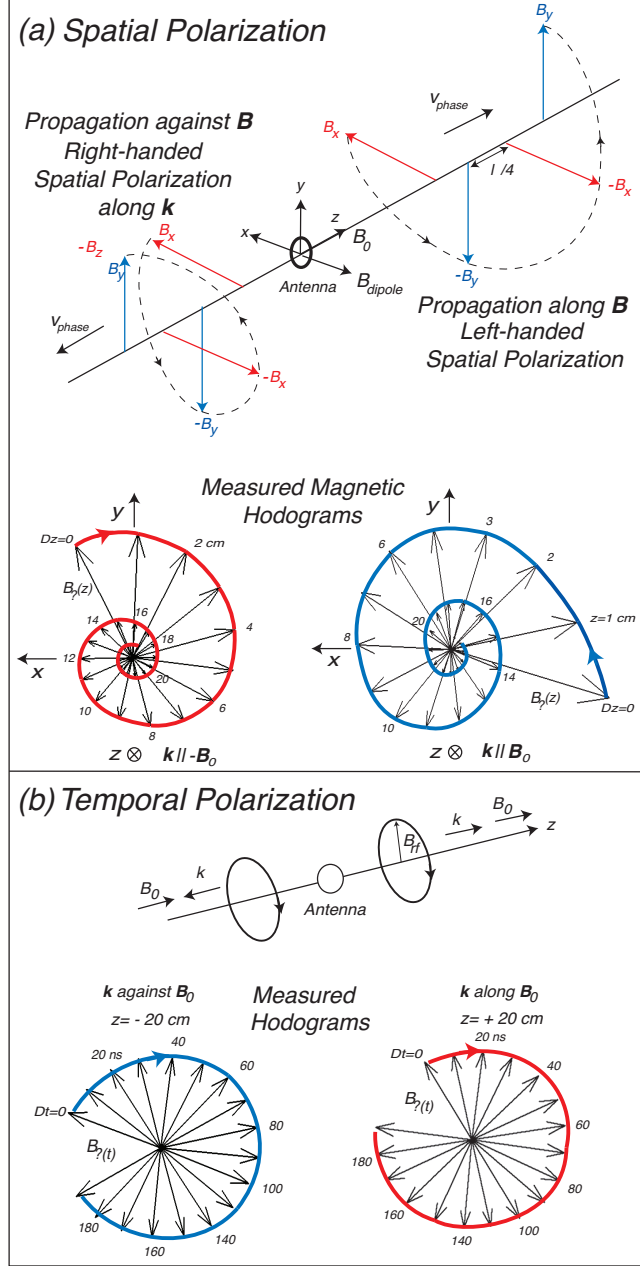


FIG. 7: Spatial and temporal polarization of whistler modes. (a) Schematic display of the field vectors along the  $z$ -axis as derived from Fig. 2(a,b). The axial hodogram of  $(B_x, B_y)$  forms a left-handed spiral in the direction of wave propagation along  $\mathbf{B}_0$  and a right handed spiral along  $\mathbf{k}$  for propagation against  $\mathbf{B}_0$ . The measured hodograms are in agreement with the schematic picture. (b) The temporal polarization is always clockwise or right-handed with respect to  $\mathbf{B}_0$  at a fixed position, irrespective of direction of wave propagation, as demonstrated by the measured hodograms.

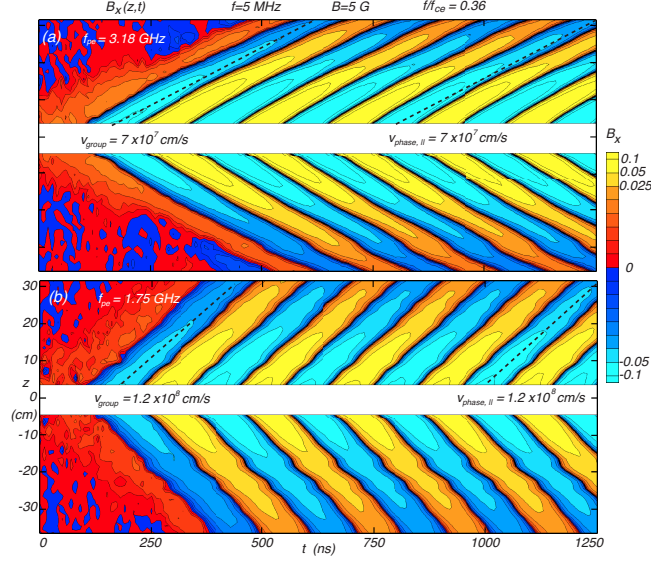


FIG. 8: Time-of-flight diagram of the wave field  $B_x(z, t)$  for  $x = y = 0$  for two different densities, (a) in the early afterglow and (b) late afterglow. The initial velocity at turn-on yields the group velocity which is identical to the parallel phase velocity for Gendrin modes. The plasma frequency is obtained from  $v_{group} = c\omega_{ce}/(2\omega_{pe})$ .



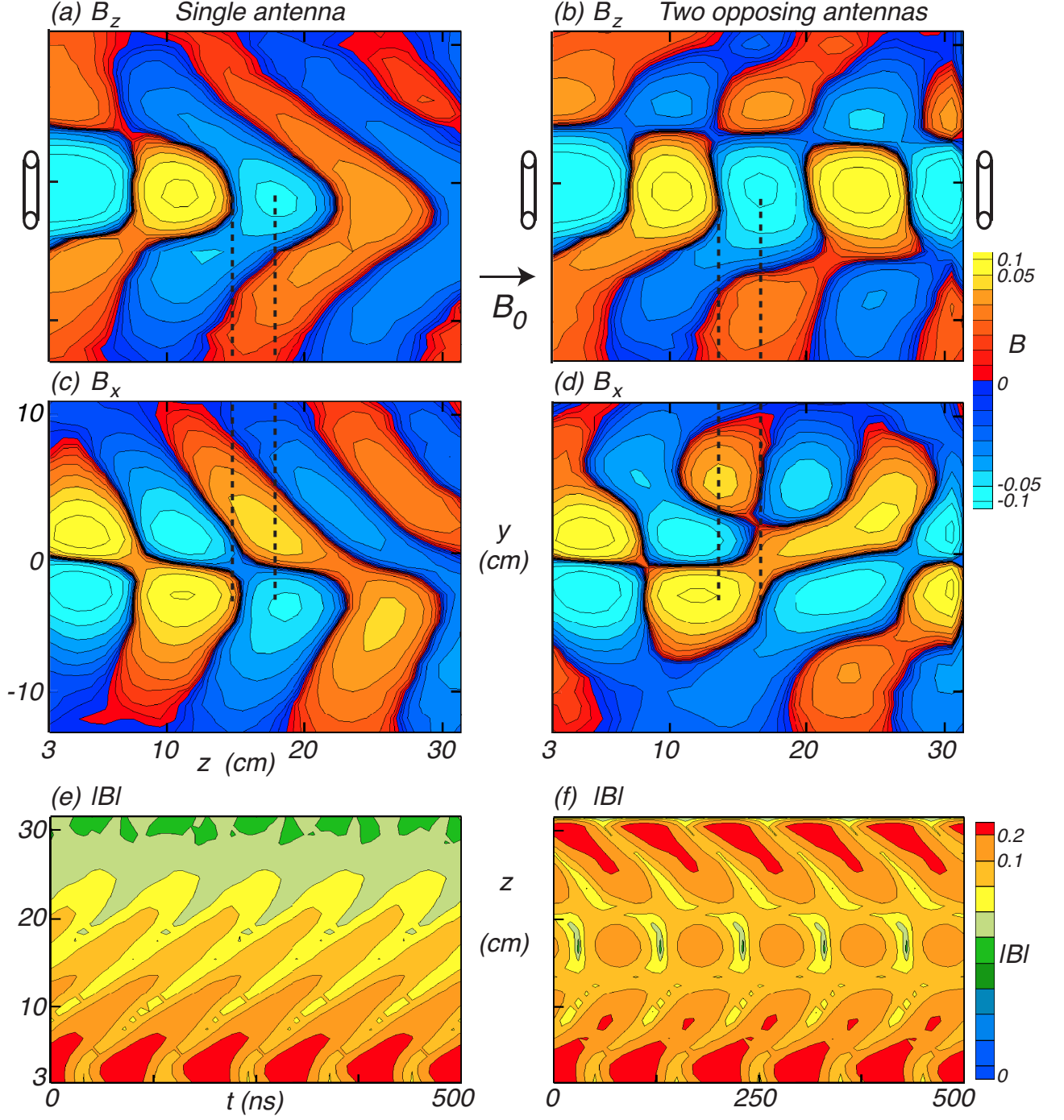


FIG. 9: Generation of standing whistler waves between two antennas with dipole axis along  $\mathbf{B}_0$ . Axial field component  $B_z$  for (a) a single loop antenna and (b) for two loops located at  $z = 0$  and  $z = 35$  cm. (c), (d) The transverse components  $B_x(y, z)$  for both cases. (e), (f) The total wave amplitudes in the  $z$ - $t$  plane ( $x \simeq y \simeq 0$ ) showing wave propagation for one antenna and standing waves for two antennas. The vertical dashed lines indicate that at the maximum of  $B_z$  the transverse field assumes a minimum and vice-versa, hence no absolute field nulls arise.



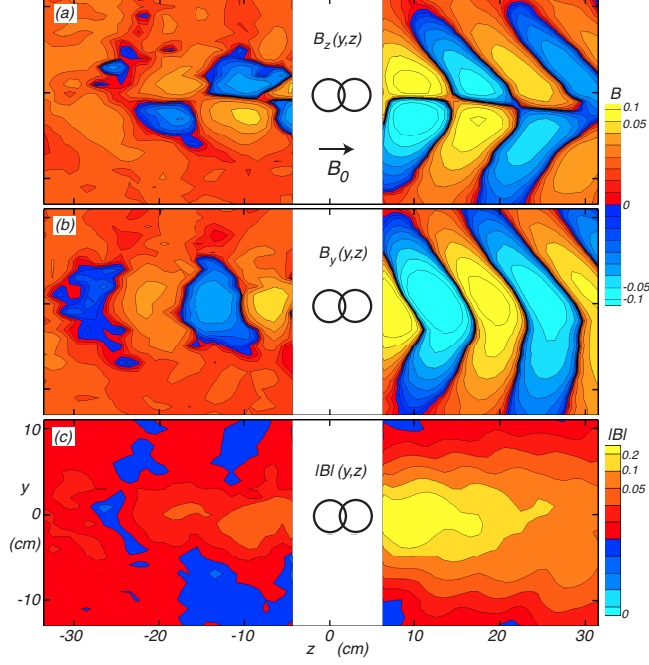


FIG. 10: Directional radiation from two loop antennas separated by  $\lambda/4$  and delayed by  $\pi/2\omega = 50$  ns. (a) Axial field component  $B_z(y, z)$ , (b) transverse field  $B_y(y, z)$ , and (c) the total field strength  $|\mathbf{B}|(y, z)$ . The antenna radiates preferentially along  $\mathbf{B}_0$ .

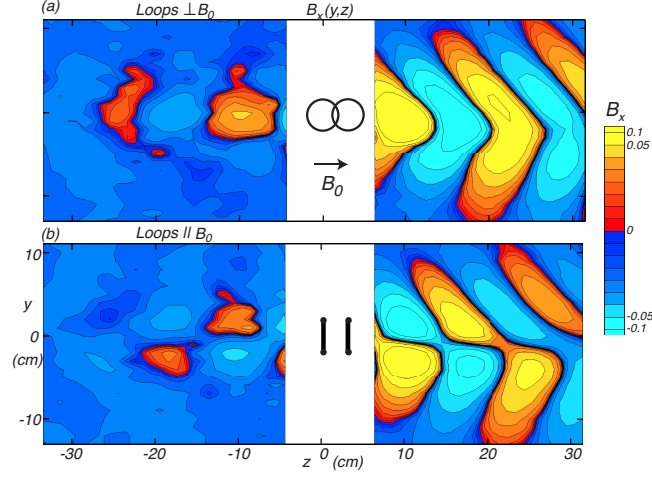


FIG. 11: Directional radiation from two phased loops with dipole moments (a) across and (b) along  $\mathbf{B}_0$ . Both cases exhibit directionality, although they have different field topologies as seen in  $B_x(y, z)$ .

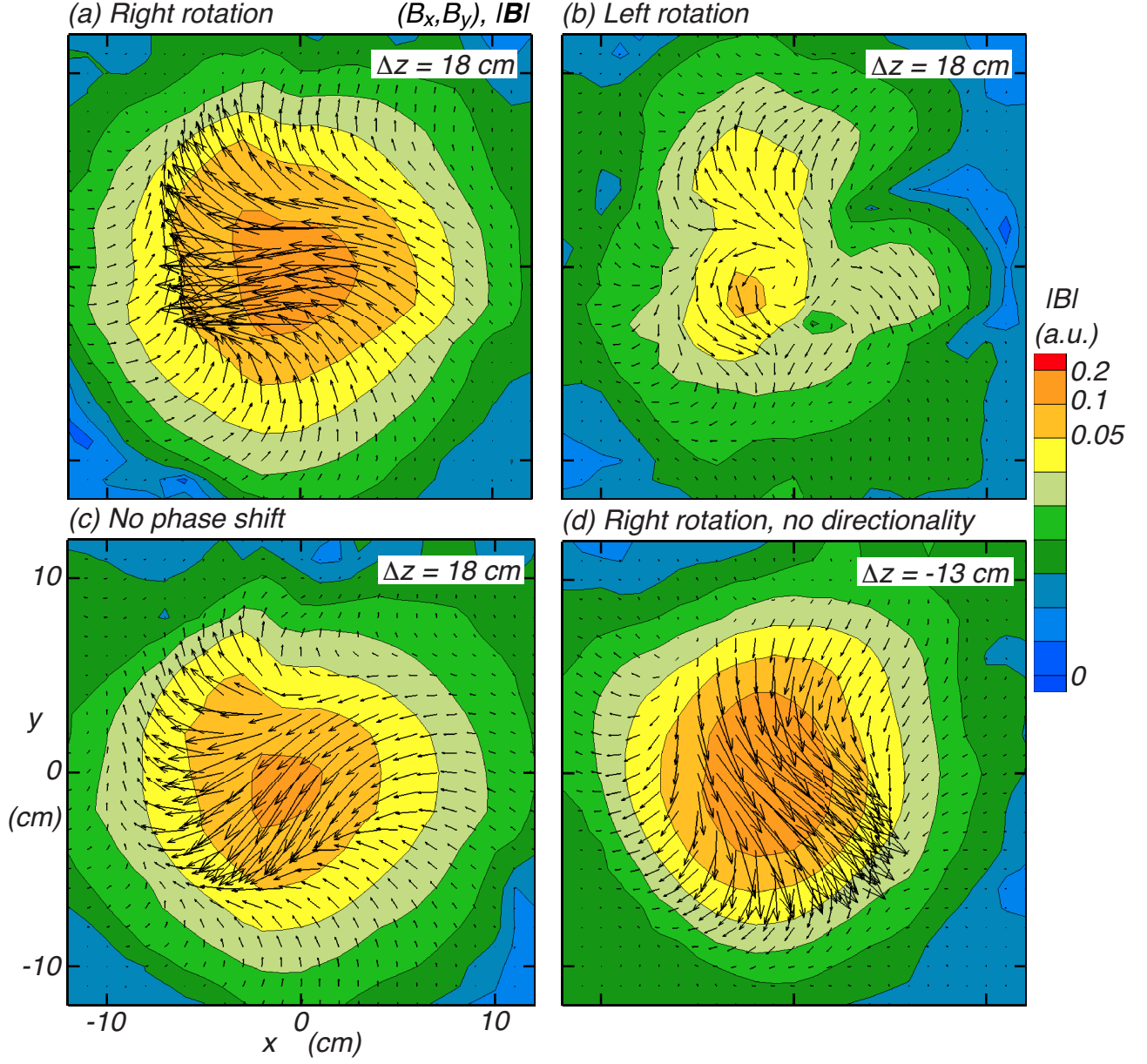


FIG. 12: Whistler modes excited by an antenna with a rotating magnetic field. Displayed are vectors of  $(B_x, B_y)$  and contours of  $|\mathbf{B}|$  in  $x$ - $y$  planes at a distance  $\Delta z = 18$  cm from the antenna. (a) Right-handed field rotation excites a strong wave field while (b) a left-handed field rotation does not couple well to whistlers with right-handed polarization. (c) Field excited by both loops in phase which produces a linear polarization at  $45^\circ$  with respect to either loop. it is almost as efficient as a rotating field antenna. (d) A strong field is also excited on the opposite side of the antenna with right-hand rotating field ( $\Delta z \simeq -13$  cm). Thus rotating antennas exhibit no directionality with respect to  $\mathbf{B}_0$ .